

Water-stable Perovskite-loaded Nanogels Containing Antioxidant Property for Highly Sensitive and Selective Detection of Roxithromycin in Animal-derived Food Products

Jinsol Han

Changwon National University

Mirkomil Sharipov

Changwon National University

Youngil Lee

University of Ulsan

Bui The Huy

Changwon National University

YONG-ILL LEE (✉ yilee@changwon.ac.kr)

Changwon National University

Soojin Hwang

Changwon National University

Research Article

Keywords: MIP nanogel, water-stable perovskite, animal-derived food, antibiotics, roxithromycin

Posted Date: August 26th, 2021

DOI: <https://doi.org/10.21203/rs.3.rs-827419/v1>

License:  This work is licensed under a Creative Commons Attribution 4.0 International License.

[Read Full License](#)

Version of Record: A version of this preprint was published at Scientific Reports on February 24th, 2022. See the published version at <https://doi.org/10.1038/s41598-022-07030-9>.

Abstract

Luminescent inorganic lead halide perovskite nanoparticles lack stability in aqueous solutions, which limits their application to optical sensors. Here, hybrid CsPbBr₃-loaded MIP nanogels were developed with enhanced stability in aqueous media. Multifunctional MIP nanogels with antioxidant function and hydrophobic cavities were synthesized from HEMA derivatives in the presence of roxithromycin as a template. The CsPbBr₃ nanoparticles were loaded into pre-synthesized MIP nanogels via in-situ synthesis with a size distribution of 200 nm. The developed CsPbBr₃-nanogel exhibit excellent stability to air/moisture and enhanced stability toward an aqueous solvent. The developed CsPbBr₃-loaded MIP nanogels showed a selective and sensitive detection of ROX with a limit of detection calculated to be 1.7×10^{-5} µg/mL (20.6 pM). The developed CsPbBr₃-loaded MIP antioxidant-nanogels were evaluated on practical application for quantitative determination of ROX antibiotic in animal-derived food products with excellent analytical performance. The detection of ROX in animal-derived food products showed good recovery results making them an ideal candidate for sensing ROX.

Introduction

Inorganic and hybrid lead halide perovskites have drawn much interest from the scientific research community owing to their outstanding electrical and optical properties (e.g., high photoluminescence quantum yield and narrow emitting bands) ¹⁻³. In addition, these types of materials have good compositional flexibility by various combinations of ions entering the crystal structure or by surface modification, the light emission spectral region can be easily adjusted in a large spectral wavelength region and the preparation costs are relatively low ^{4,5}. Despite these excellent properties, perovskite nanoparticles have low stability to environmental factors such as temperature, pressure, solvent and have more importantly high sensitivity to moisture and oxygen, which hold back all sensing application that involves the use of water ⁶⁻¹⁰. The fast dissociation and the loss of optical properties of these materials having in contact with highly polar solvents including water are caused by intrinsic ionic properties ¹¹. Other important issues of perovskite is the oxidation ¹² and thermal instability ¹³. Qidong Tai et al. have achieved high stability of tin-based perovskite FASnI₃ for solar cells via the introduction of hydroxybenzene sulfonic acid or salt to prevent the oxidation of Sn²⁺ ions to Sn⁴⁺ upon oxygen-air exposure ¹⁴. Although cesium lead halide perovskites are relatively less sensitive to oxygen compared to tin-based perovskites they still lack the stability toward oxygen ¹².

Nanogels, one type of polymeric material in which the hydrophilic function renders them capable of carrying large amounts of water molecules in their 3D networks ¹⁵⁻¹⁷. During the last decades, poly(2-hydroxyethyl methacrylate) (PHEMA)-based nanogels have been widely used for the development of biomedical products due to their excellent biocompatibility ¹⁸ and dimension stability ¹⁹. Additionally, molecularly imprinted polymer (MIP) nanogels have a very good performance in selective binding and absorption of analytes in high concentrations due to their swelling capabilities. Various nanoparticles

including gold, silver, magnetic, and upconversion nanoparticles have been successfully coated with MIPs for nanomedicinal and sensing applications ^{15,20}.

Recently, the studies of microbiome indicated that antibiotics present in animal-derived food cause dysregulation of gut microbiota ^{21,22} and increase the resistance to antibiotics which was classed as one of the most terrible global threats of the twenty-first century ²³. Roxithromycin (ROX) is a semi-synthetic macrolide antibiotic with 14-membered macrocyclic lactone ring and shows 1–4 times stronger in-vivo antibacterial effect to that of erythromycin ²⁴. ROX has a high degree of antibacterial activity against both Gram-positive and Gram-negative bacteria ²⁵. ROX is rapidly absorbed, has a long half-life of elimination, and has great biological activity against Streptococcus, Staphylococcus aureus, Listeria, and Corynebacterium bacteria ²⁶. Although these advantages of ROX and other macrolides make them attractive in veterinary practice for use in the prevention and treatment of bacterial pathogens, abusive and unsafe use of macrolides antibiotics in farms can lead to the accumulation of macrolides and their residues in food products derived from animals, thereby causing allergic reactions or toxic effects on consumers ²⁷. Thus far, various analytical approaches for detecting antibiotics in animal-derived food products have been developed, such as rotating-disk sorptive extraction and liquid chromatography ²⁸, electrophoresis ²⁹, desorption corona beam ionization coupled mass spectrometry ³⁰, and microbiological assays ³¹. Microbiology assays lack selectivity and sensitivity. Contrarily, mass spectrometry techniques are selective and sensitive, however, they require complicated sample pretreatment, expensive instrumentations, and well-trained personnel.

Here, we have developed a novel CsPbBr₃-loaded PHEMA MIP nanogel for the first time with high stability against water and oxidation. The method stands out due to the multifunctional MIP nanogel synthesized from four 2-(hydroxyethyl)methacrylate (HEMA) derivatives with different functions: a) gallic-(hydroxyethyl)methacrylate ester (GA-HEMA) and caffeic-(hydroxyethyl)methacrylate ester (CA-HEMA) monomers are synthesized from naturally available gallic and caffeic acids with antioxidant property that increases the stability of loaded perovskites toward oxygen species and oxidizing agents; b) oleic-(hydroxyethyl)methacrylate ester (OA-HEMA) allows the formation of hydrophobic cavities that will further serve as CsPbBr₃ perovskites reservoirs; c) polyethylene glycol-(hydroxyethyl)methacrylate ester (PEG-HEMA) increases the hydrophilicity of nanogels to reduce non-specific interactions thus resulting in higher dispersion and lower interaction with non-imprinted molecules and macromolecules. Bearing in mind that CsPbBr₃ are sensitive to water, MIP antioxidant-nanogels were first prepared with ROX as a template and perovskite nanoparticles were loaded into nanogels via in-situ synthesis through hot-injection method. Developed MIP antioxidant-nanogels loaded with CsPbBr₃ perovskite nanoparticles showed enhanced stability for water and polar solvents owing to the swelling properties of nanogel that allows the absorption of water molecules into three-dimensional networks of the polymer. Finally, the developed CsPbBr₃-loaded MIP antioxidant-nanogels were successfully applied for the selective and sensitive detection of ROX antibiotic in animal-derived food products.

Results And Discussion

Multifunctional MIP nanogels

To develop multifunctional MIP nanogels and grant enhanced stability to CsPbBr₃ perovskites toward water and oxygen, three HEMA derivatives were synthesized. The HEMA derivatives GA-HEMA, CA-HEMA, and OA-HEMA have been synthesized through Steglich esterification method as shown in Fig. 1a. GA-HEMA, CA-HEMA, and OA-HEMA were obtained in form of brown, yellow, and transparent oils, respectively. Three monomers were characterized by ¹H-NMR and FT-IR techniques with the discussion presented in supporting information and **Figure S1**. Multifunctional MIP nanogels were prepared via surfactant-free emulsion polymerization method using four HEMA derivatives: GA-HEMA, CA-HEMA, OA-HEMA, and PEG-HEMA in the presence of ROX as a template, as shown in Fig. 1b. Afterward, CsPbBr₃ perovskite nanoparticles were loaded via in-situ synthesis for selective detection of ROX, as shown in Fig. 1c-d. The FT-IR spectrum of MIP nanogels showed a strong absorption peak at 1730 cm⁻¹, attributed to the characteristic C = O stretch of the ester group and a strong peak located at 1640 cm⁻¹, associated with conjugated C = C group of the aromatic groups as shown in Fig. 2a. Moreover, the two absorption peaks at 1250 cm⁻¹ and 1167 cm⁻¹ are attributed to the characteristic C-O stretch of ester and PEG. Finally, the relatively strong peak at 2940 cm⁻¹ is caused by sp³ C-H stretching from oleic acid. To confirm a successful polymerization, the molecular weight of nanogel was measured via gel permeation chromatography (GPC) technique, as illustrated in **Figure S2**. The average molecular weight (M_w) of MIP nanogels were found to be 14,820 g/mol with a polydispersity (M_w/M_n) equal to 1.25. Whereas, a non-imprinted polymer had an average M_w of 15,850 g/mol, and polydispersity (M_w/M_n) was 1.21. This result confirms that the presence of ROX during the polymerization step does not affect the polymerization rate and the template was successfully removed. To confirm the successful imprinting of ROX in nanogels, UV-vis absorption was measured. As illustrated in Fig. 2b, ROX has an absorption peak located at 211 nm which was greatly decreased after washing MIP with water several times. These results confirm the successful removal of the ROX template from MIP. The morphology and the size of MIP nanogels were studied through FE-SEM images (Fig. 2c-d). MIP nanogels have a well-defined spherical shape with a size distribution of 300 nm. It is worthy to note that the majority of MIP nanogels are aggregated together in a well-dried state, as shown in **Figure S3a**, due to polymeric nature. However, after the addition of ethanol/water mixture, these MIP nanogels disperse and swell to reach a size ranged from 700 nm to 900 nm (**Figure S3b**).

Perovskite-loaded MIP nanogels

Cesium lead bromide perovskite nanoparticles were loaded into MIP nanogel through in-situ synthesis by hot-injection approach. First MIP nanogels were dispersed in ethanol and added to the PbBr₂ precursor solution and heated at 120°C to evaporate ethanol and to distribute the PbBr₂ precursor in nanogel cavities. In the second step, the cesium oleate precursor solution was mixed with MIP/PbBr₂ via hot-injection method to form CsPbBr₃ perovskite nanoparticles loaded in hydrophobic cavities. To confirm the

successful formation of CsPbBr₃ perovskite nanoparticles, X-ray diffraction (XRD) analysis was performed, as shown in Fig. 3a. The synthesized perovskites have a crystal structure in which a tetragonal system is present [mp-1014168, Materials Project data repository]. The diffraction peaks at $2\theta = 14.94^\circ, 21.05^\circ, 29.95^\circ, 36.90^\circ, \text{ and } 42.61^\circ$ are ascribed to the tetragonal CsPbBr₃ lattices planes (110), (112), (220), (312), and (224), respectively. However, XRD patterns also indicate the transformation of the small quantity of CsPbBr₃ into a CsBr-rich non-perovskite rhombohedral Cs₄PbBr₆ (JCPDS card no. 01-073-2478) phase probably due to the accumulation of Cs ions on more accessible locations during the second step of hot-injection method. This transformation has been already observed during the synthesis with an excess of CsBr [8]. Due to fast reaction rate, the CsCO₃ precursor does not have enough time to spread evenly, which results in the accumulation of Cs ions in a certain location, leading to the formation of CsBr-rich non-perovskite rhombohedral Cs₄PbBr₆ nanoparticles. To study the morphology of MIP/CsPbBr₃, FE-SEM analysis was performed. As shown in Fig. 3b and **Figure S4**, MIP nanogels were successfully loaded with perovskite nanoparticles with a size distribution of 200 nm while the size of nanogels has increased to around 900 nm due to swelling properties. In addition, we could confirm the successful loading of CsPbBr₃ nanoparticles into the nanogel by the presence of cesium, lead, and bromine atoms in energy dispersive X-ray spectrum, as shown in **Figure S5**. Initially, nanogels were synthesized only from CA-HEMA, GA-HEMA, and OA-HEMA monomers. However, the formed nanogels showed low water dispersibility which further influenced the fluorescence stability of MIP/CsPbBr₃. As shown in Fig. 3c, the loading of perovskite nanoparticles in such nanogels has increased the water stability as expected, but the absence of hydrophilic function resulted in low dispersibility and fast aggregation of MIP/CsPbBr₃. To increase the dispersibility and the accuracy of photoluminescence measurements, commercially available PEG-HEMA monomer was introduced. Owing to hydrophilic property and low non-specific interaction of PEG-HEMA, it enabled a better dispersibility and lower aggregation rate of nanogel. Moreover, the water stability of perovskite was further improved, and the intensity of fluorescence was increased during the first hour (Fig. 3d). A similar phenomenon was observed by Qixuan Zhong et al. after coating perovskite nanoparticles with silica shell which allowed better dispersion in water resulting in higher photoluminescence³². The good stability of MIP/CsPbBr₃ can be explained by the insertion of perovskite nanoparticles in hydrophobic cavities of nanogel during the hot-injection method. Moreover, nanogels are composed of three-dimensional polymeric networks that absorb the water thus lowering the contact of water molecules with perovskite nanoparticles. Finally, GA-HEMA and CA-HEMA act as an antioxidant to reduce the oxidation of perovskite by oxygen species.

Sensitivity of ROX Detection

The fluorescence response of the MIP/CsPbBr₃ (0.001 ppm) was studied upon the addition of increasing the concentrations of ROX between 1×10^{-6} and 1×10^{-10} M and shown in Fig. 4a. The fluorescence intensities of perovskite solution decreased gradually with an increase in ROX concentration, because of the tailor-made recognition sites of the MIP/CsPbBr₃ specific to ROX. As illustrated in Fig. 4b, the F_0/F value represents a linear relationship with the concentration of ROX ranged from 1×10^{-6} M to 1×10^{-10} M with a good linear correlation coefficient (0.995) and low detection limit (2.06×10^{-11} M). The limit of

detection was determined by the following equation. $LOD=10 \left[\frac{\log(3\sigma+y_0) - a}{b} \right]$, where a is the intercept of fitted line, b is the slope of fitted line, σ is the standard deviation of the blank intensities of the perovskite solution and y_0 is the mean of blank intensities of the perovskite solution ($n = 3$). In order to confirm the formation of specific recognition sites to ROX within MIP nanogels, detection of the different concentrations of ROX using the perovskite-loaded nonimprinted polymer (NIP) nanogels was performed. In the case of NIP, a slight change in the fluorescence intensity of perovskite has been observed, which is explained by minor quenching of more accessible perovskite particles located near the surface by water or by ROX. However, compared to the MIP, the changes in fluorescence intensity were insignificant according to the concentration of the ROX (Fig. 4c). These results demonstrate that the developed MIP/CsPbBr₃ particles have great properties to detect ROX with high sensitivity.

Selectivity of ROX Detection

Selectivity tests were performed to evaluate whether the developed MIP/perovskite can selectively detect only ROX among various antibiotics and common tripeptide Glutathione (Fig. 4d). Four different antibiotics (Azithromycin, Chloramphenicol, Ciprofloxacin, and ROX) were selected as analytes and prepared in ethanol/water at a concentration of 1 mM (Fig. 4d). As shown in Fig. 4e, non-macrolide antibiotics, such as chloramphenicol and ciprofloxacin did not affect the fluorescence intensity of the developed sensor, while azithromycin which has structural similarities to ROX induced a slight decrease in fluorescence intensity. Bearing in mind that this sensor has a potential in the analysis of animal-derived food products that contain different proteins, the selectivity to common tripeptide glutathione was investigated. A slight quenching of MIP/CsPbBr₃ observed in the presence of glutathione can be explained by the transformation of CsPbBr₃ into non-luminescent phase. A similar phenomenon was observed in previously reported work, where CsPbBr₃ was transformed into non-luminescent Cs₄PbBr₆ in the presence of thiol-alkyl and residual oleylamine³³. In contrast to tested molecules, ROX exhibited significant quenching efficiency more than 2-fold, thus confirming the efficient selectivity of the developed sensor towards ROX.

Mechanism of ROX Detection

Different quenching mechanisms have been considered, including molecular interactions by electrostatic or hydrogen bonding between analyte and perovskite, Förster resonance energy transfer (FRET), inner filter effect (IFE), and perovskite phase transformation or oxidation. In the FRET mechanism, the collision during dynamic quenching between the fluorescent material in an excited state and the quencher molecule results in loss of energy and return to the ground state. Moreover, it requires that the emission spectrum of the energy donor must overlap with the absorption spectrum of the energy acceptor. The synthesized MIP/CsPbBr₃ have a typical peak emission of cesium lead bromide at 520 nm, whereas the ROX absorption peak is at 221 nm, as shown in Fig. 5a. These results suggest the absence of spectral overlap between perovskite and ROX; therefore, the probability of energy transfer in the fluorescence quenching mechanism is very minuscule. Thus, possible quenching mechanisms are either phase

transformation or the oxidation of perovskite by ROX. In the case of NIP to which ROX is not added as a template molecule in the polymerization process, no cavity complementary to ROX exists in the polymer. Therefore, even if ROX is added during the detection process, it cannot bind to ROX, and the fluorescent emission of perovskite is not affected. However, in the case of MIP to which ROX is added as a template molecule in the polymerization process, a cavity complementary to ROX exists within the nanogel. Thereby, during the detection process, ROX binds to the cavity in the polymer, and structural decomposition of perovskite is induced by the N-oxime functional group having the oxidative property of ROX. Subsequently, the decomposition of CsPbBr₃ nanoparticles results in a decrease in fluorescence (Fig. 5b).

Practical Application of the Sensor for Animal-derived Food Products

The practical relevance of perovskite-loaded MIP nanogels for the detection of ROX was investigated in three animal derived-food products: meat, milk, and egg. Pork meat, eggs, and milk products were acquired from local grocery stores in Changwon, Republic of Korea. Prior analysis, samples were extracted by experimental procedure reported in previous works and spiked with ROX standard solution³⁴. Acceptable recoveries and relative standard deviations (RSDs) of ROX spiked in milk, porcine muscle, and egg samples using MIP/CsPbBr₃ have been achieved, as shown in Table 1. The recoveries of ROX ranged from 99.2 ~ 100 %, 101 ~ 102 %, and 98.2 ~ 99.1 %, with RSDs, ranged from 6.32 ~ 11.7 %, 3.66 ~ 6.99 %, and 5.84 ~ 6.46 % for milk, pork, and eggs, respectively. These findings demonstrate the accuracy of the developed sensor for selective and sensitive detection of ROX in animal-derived food samples, thus revealing the good potential for practical application. The analytical performances of the synthesized MIP/CsPbBr₃ for detecting ROX were compared to several methods previously reported. As shown in Table 2, most reported methods require sophisticated sample treatment, good technicians, and long analysis time. By contrast, our developed fluorescence sensor does not require expensive instruments and long analysis time, and shows excellent analytical performance with wide dynamic range from 8.4×10^{-5} to 8.4×10^{-1} µg/mL and lower detection limit of 1.7×10^{-5} µg/mL (20.6 pM) compared with those in the previously reported sensing methods.

Table 1
Results of ROX detection in milk, pork, and eggs real samples by developed MIP/perovskites.

Samples	Added ($\times 10^{-5}$ M)	Found ($\times 10^{-5}$ M)	Recovery (%)	RSD (n = 3, %)
Milk	1.00×10^{-3}	$0.99 \pm 0.09 \times 10^3$	99.3	9.32
	1.00×10^{-1}	$0.99 \pm 0.11 \times 10^1$	99.2	11.7
	1.00×10	$1.00 \pm 0.06 \times 10$	100	6.32
Pork	1.00×10^{-3}	$1.02 \pm 0.03 \times 10^3$	102	3.66
	1.00×10^{-1}	$1.03 \pm 0.07 \times 10^1$	102	6.99
	1.00×10	$1.01 \pm 0.04 \times 10$	101	4.72
Eggs	1.00×10^{-3}	$0.99 \pm 0.06 \times 10^3$	99.1	6.46
	1.00×10^{-1}	$0.99 \pm 0.06 \times 10^1$	98.7	6.07
	1.00×10	$0.98 \pm 0.05 \times 10$	98.2	5.84

Table 2
Comparison of CsPbBr₃-loaded MIP nanogels with other general methods for the detection of ROX.

Analytical technique	Linear Range ($\mu\text{g/mL}$)	LOD ($\mu\text{g/mL}$)	References
1 High-performance liquid chromatography (HPLC)	0.05–20.0	5.0×10^{-2}	37
2 Electrochemistry (EC)	4.2–84	4.0×10^{-1}	38
3 Fluorescence using CdTe quantum dots (FL)	25.0-350.0	4.6	39
4 Aqueous two-phase system extraction (ATPSE)	1.0–20.0	3.0×10^{-2}	40
5 Capillary electrophoresis (CE)	0.02–201.0	7.0×10^{-3}	29
6 Fluorescence using MIP/CsPbBr ₃ (FL)	8.4×10^{-5} - 8.4×10^{-1}	1.7×10^{-5}	This Study

Conclusion

In conclusion, CsPbBr₃-loaded MIP nanogel with water and oxygen stability was developed via in-situ synthesis of cesium lead bromide. Multifunctional MIP nanogel with antioxidant property showed enhanced stability of CsPbBr₃ nanoparticles in water. MIP nanogels showed highly sensitive and

selective detection of imprinted macrolide ROX with a wide dynamic range and a low limit of detection calculated to be 20.6 pM. Moreover, the detection of ROX via the developed sensor in animal-derived food products showed its high potential for practical application with good recoveries and acceptable RSDs. We believe that the achieved stability of CsPbBr₃-loaded nanogels will also inspire researchers in the development of new hybrid nanomaterials for not only sensing applications, but also in the development of novel solar cell technologies and LEDs.

Methods

Materials and Characterization Methods

The chemicals and characterization methods are described in supporting information.

Esterification of gallic, caffeic, and oleic acid

GA-HEMA

Monomers were synthesized via Steglich esterification method with small modifications³⁵. Briefly, to the precooled solution at 0°C containing gallic acid (1.00 g, 5.88 mmol, 1 eq) and HEMA (1.53 g, 11.8 mmol, 2 eq) in tetrahydrofuran (THF) (40 mL), an activator N,N'-dicyclohexylcarbodiimide (DCC) was added dropwise (1.21 g, 5.88 mmol, 1 eq) in THF (10 mL). The mixture was continuously stirred for 30 min at 0°C, then added 4-(N,N-dimethylamino)-pyridine (DMAP) catalyst (0.0718 g, 0.59 mmol, 0.1 eq), and stirred again for next 24 h at 0°C, then allowed to reach room temperature. The precipitate was filtered out when the reaction was finished to remove N,N'-dicyclohexylurea (DCU), and the substance was concentrated under reduced pressure. The oily product was poured into a mixture of chloroform and isopropanol (CHCl₃:C₃H₈O = 3:1, v/v). To remove the catalyst and DCU residues the organic layer was repeatedly washed with 1 M HCl solution, then with saturated aqueous sodium bicarbonate solution, with brine solution, and finally with deionized water. The solvent was removed under reduced pressure and the product was further purified by adding cold diethyl ether (0°C) to filter out catalysts with poor solubility in the cold solvent. The purified compound was analyzed by proton nuclear magnetic resonance (¹H NMR) spectrometer and Fourier transform infrared (FTIR) spectrometer.

CA-HEMA

CA-HEMA was synthesized through the same experimental protocol with minor changes in purification steps. After removal of catalyst and DCU residual by washing step, the organic layer was concentrated under reduced pressure and the product was further purified by adding cold acetone (0°C) to filter out catalysts with poor solubility in the cold acetone solvent. CA-HEMA was characterized via ¹H NMR and FT-IR.

OA-HEMA

OA-HEMA was synthesized via the same experimental procedure used for the synthesis of GA-HEMA with a minor modification in the synthesis step. The solvent, THF was replaced by dichloromethane (DCM) due to the better solubility of reactants in DCM. Briefly, To the precooled solution at 0°C, containing oleic acid (1.66 g, 5.88 mmol, 1 eq) and HEMA (1.53 g, 11.8 mmol, 2 eq) in DCM (40 mL), activator DCC was added dropwise (1.21 g, 5.88 mol, 1 eq) in DCM (10 mL). The mixture was continuously stirred for 30 min at 0°C, then added DMAP catalyst (0.0718 g, 0.59 mmol, 0.1 eq), and stirred again for the next 24 h at 0°C and allowed to reach room temperature. The product was purified and characterized through the same procedures and techniques described in previous sections.

Synthesis of antioxidant MIP nanogels

Nanogels were synthesized via surfactant-free emulsion polymerization method reported previously with minor modifications³⁶. The poly(vinyl alcohol) (0.5 g), was fully dissolved in 50 ml water/THF solvent (4:1, v/v) to form a continuous phase. Then, the mixture of GA-HEMA, CA-HEMA, OA-HEMA, PEG-HEMA, and EGDMA (0.82 mmol, 0.82 mmol, 0.82 mmol, 2.46 mmol, and 0.05 mmol, respectively) were added to the dispersion under ultrasonication and kept for an additional half an hour. In the case of MIP, 1 mmol ROX (template) was dissolved in the solution. Ammonium persulphate was used as an initiator with a concentration of 0.44 mg/ml in monomer phase. Firstly, the initiator was added to the reaction mixture and nitrogen gas was bubbled for approximately 1–2 min under stirring to remove dissolved oxygen. Afterward, the solution was stirred at 70°C for 24 h under nitrogen atmosphere. Upon the completion of polymerization, nanogels were collected by centrifugation at 15,000 rpm for 30 min and resuspended in ethanol/water (1:1). This procedure was repeated several times to eliminate the unreacted monomer, initiator, and template analyte.

Loading CsPbBr₃ perovskites in MIP nanogels by hot-injection method

Firstly, cesium oleate was prepared by stirring cesium carbonate (0.25 mmol) and 0.25 mL of oleic acid in 4 mL of 1-octadecene (ODE) under nitrogen gas at 120°C for 1 h in a 3-neck flask. Separately, lead(II) oxide (0.188 mmol), ammonium bromide (0.585 mmol), 0.5 mL of oleic acid, and 0.5 mL of oleylamine as a capping ligand are added in 5 mL of ODE under nitrogen gas to fully dissolve the lead halide. The temperature is raised and kept at 120°C for 30 min in vacuo. When this solution becomes transparent, 0.1 g of MIP nanogel in 1 mL of ethanol is injected, and ethanol was evaporated by heating for about 30 min. Afterward, the cesium oleate solution at 120°C is swiftly injected and the mixture stirred for 5–10 seconds before quenching the reaction in an ice-water bath (0°C). MIP nanogel loaded with perovskite nanoparticles were poured in ethyl acetate and collected by centrifugation at 10,000 rpm for 10 min.

Abbreviations

¹H NMR: Proton Nuclear Magnetic Resonance

CA-HEMA: Caffeic-(hydroxyethyl)methacrylate ester

DCC: N,N'-dicyclohexylcarbodiimide

DCM: Dichloromethane

DCU: N,N'-dicyclohexylurea

DMAP: 4-(N,N-dimethylamino)-pyridine

FRET: Förster resonance energy transfer

FT-IR: Fourier Transform Infrared

GA-HEMA: Gallic-(hydroxyethyl)methacrylate ester

GPC: Gel permeation chromatography

HEMA: (2-hydroxyethyl methacrylate)

IFE: Inner filter effect

MIP: Molecularly imprinted polymer

MIP/CsPbBr₃: Cesium lead bromide perovskite-loaded MIP nanogels

NIP: Nonimprinted polymer

OA-HEMA: Oleic-(hydroxyethyl)methacrylate ester

ODE: 1-octadecene

PEG-HEMA: Polyethylene glycol-(hydroxyethyl)methacrylate ester

PHEMA: Poly(2-hydroxyethyl methacrylate)

ROX: Roxithromycin

THF: Tetrahydrofuran

XRD: X-ray diffraction

Declarations

Acknowledgements

This work was supported by the Basic Science Research Program (NRF-2018R1A2B6001489 and NRF-2020R1A2C2007028) through the National Research Foundation of Korea.

Availability of data and materials

The datasets used and/or analysed during the current study are available from the corresponding author on reasonable request.

Competing interests

The authors declare that they have no competing interests.

Author's Information

Jinsol Han and Mirkomil Sharipov contributed equally.

Affiliations

Department of Chemistry, Changwon National University, Changwon 51140, Republic of Korea.

Jinsol Han, Mirkomil Sharipov, Bui The Huy & Yong-Il Lee

Department of Chemistry, University of Ulsan, Ulsan 44776, Republic of Korea.

Mirkomil Sharipov & Youngil Lee

Funding

This work was supported by the Basic Science Research Program (NRF-2018R1A2B6001489 and NRF-2020R1A2C2007028) through the National Research Foundation of Korea.

Authors' contributions

JH: conceptualization, investigation, validation, formal analysis

MS and SH : conceptualization, methodology, investigation, writing- original draft

BTH: methodology

YL: conceptualization, supervision, funding acquisition

Y-IL: conceptualization, supervision, writing-review & editing, funding acquisition

Corresponding authors

Correspondance to Youngil Lee or Yong-Il Lee.

References

1. Docampo, P., Bein, T. A. & Long-Term View on Perovskite Optoelectronics. *Acc. Chem. Res*, **49**, 339–346 <https://doi.org/10.1021/acs.accounts.5b00465> (2016).
2. Manser, J. S., Christians, J. A. & Kamat, P. V. Intriguing Optoelectronic Properties of Metal Halide Perovskites. *Chem. Rev*, **116**, 12956–13008 <https://doi.org/10.1021/acs.chemrev.6b00136> (2016).
3. Stoumpos, C. C. *et al.* Crystal Growth of the Perovskite Semiconductor CsPbBr₃: A New Material for High-Energy Radiation Detection. *Cryst. Growth Des*, **13**, 2722–2727 <https://doi.org/10.1021/cg400645t> (2013).
4. Protesescu, L. *et al.* Nanocrystals of Cesium Lead Halide Perovskites (CsPbX₃, X = Cl, Br, and I): Novel Optoelectronic Materials Showing Bright Emission with Wide Color Gamut. *Nano Lett*, **15**, 3692–3696 <https://doi.org/10.1021/nl5048779> (2015).
5. Xiao, H. *et al.* Polymer ligands induced remarkable spectral shifts in all-inorganic lead halide perovskite nanocrystals. *J. Mater. Chem. C*, **8**, 9968–9974 <https://doi.org/10.1039/D0TC01822H> (2020).
6. Jong, U. G. *et al.* Influence of water intercalation and hydration on chemical decomposition and ion transport in methylammonium lead halide perovskites. *J. Mater. Chem. A*, **6**, 1067–1074 <https://doi.org/10.1039/C7TA09112E> (2018).
7. Li, D. *et al.* Improving Stability of Cesium Lead Iodide Perovskite Nanocrystals by Solution Surface Treatments. *ACS Omega*, **5**, 18013–18020 <https://doi.org/10.1021/acsomega.0c01403> (2020).
8. Li, X. *et al.* All-Inorganic CsPbBr₃ Perovskite Solar Cells with 10.45% Efficiency by Evaporation-Assisted Deposition and Setting Intermediate Energy Levels. *ACS Appl. Mater. Interfaces*, **11**, 29746–29752 <https://doi.org/10.1021/acsami.9b06356> (2019).
9. Nenon, D. P. *et al.* Structural and chemical evolution of methylammonium lead halide perovskites during thermal processing from solution. *Energy Environ. Sci*, **9**, 2072–2082 <https://doi.org/10.1039/C6EE01047D> (2016).
10. Wang, W., Deng, P., Liu, X., Ma, Y. & Yan, Y. A CsPbBr₃ quantum dots/ultra-thin BN fluorescence sensor for stability and highly sensitive detection of tetracycline. *Microchem. J*, **162**, 105876 <https://doi.org/10.1016/j.microc.2020.105876> (2021).
11. De Roo, J. *et al.* Highly Dynamic Ligand Binding and Light Absorption Coefficient of Cesium Lead Bromide Perovskite Nanocrystals. *ACS Nano*, **10**, 2071–2081 <https://doi.org/10.1021/acsnano.5b06295> (2016).
12. Yang, D. *et al.* All-inorganic cesium lead halide perovskite nanocrystals: synthesis, surface engineering and applications. *J. Mater. Chem. C*, **7**, 757–789 <https://doi.org/10.1039/C8TC04381G> (2019).
13. Chaudhary, B. *et al.* Mixed-Dimensional Naphthylmethylammonium-Methylammonium Lead Iodide Perovskites with Improved Thermal Stability. *Sci. Rep*, **10**, 429 <https://doi.org/10.1038/s41598-019-57015-4> (2020).
14. Tai, Q. *et al.* Antioxidant Grain Passivation for Air-Stable Tin-Based Perovskite Solar Cells. *Angew. Chem. Int. Ed*, **58**, 806–810 <https://doi.org/10.1002/anie.201811539> (2019).

15. Molina, M. *et al.* Stimuli-responsive nanogel composites and their application in nanomedicine. *Chem. Soc. Rev*, **44**, 6161–6186 <https://doi.org/10.1039/C5CS00199D> (2015).
16. Sasaki, Y. & Akiyoshi, K. Nanogel engineering for new nanobiomaterials: from chaperoning engineering to biomedical applications. *Chem. Rec*, **10**, 366–376 <https://doi.org/10.1002/tcr.201000008> (2010).
17. Dinari, A., Abdollahi, M. & Sadeghizadeh, M. Design and fabrication of dual responsive lignin-based nanogel via “grafting from” atom transfer radical polymerization for curcumin loading and release. *Sci. Rep.* **11** 1962, doi:<https://doi.org/10.1038/s41598-021-81393-3> (2021).
18. Kopeček, J. Hydrogel biomaterials: A smart future?, **28**, 5185–5192 <https://doi.org/10.1016/j.biomaterials.2007.07.044> (2007).
19. Gaharwar, A. K., Peppas, N. A. & Khademhosseini, A. Nanocomposite hydrogels for biomedical applications. *Biotechnol. Bioeng*, **111**, 441–453 <https://doi.org/10.1002/bit.25160> (2014).
20. Elmasry, M. R., Tawfik, S. M., Kattaev, N. & Lee, Y. I. Ultrasensitive detection and removal of carbamazepine in wastewater using UCNPs functionalized with thin-shell MIPs. *Microchem. J*, **170**, 106674 <https://doi.org/10.1016/j.microc.2021.106674> (2021).
21. Tapiainen, T. *et al.* Impact of intrapartum and postnatal antibiotics on the gut microbiome and emergence of antimicrobial resistance in infants. *Sci. Rep*, **9**, 10635 <https://doi.org/10.1038/s41598-019-46964-5> (2019).
22. Nogacka, A. M. *et al.* Early microbiota, antibiotics and health. *Cell. Mol. Life Sci*, **75**, 83–91 <https://doi.org/10.1007/s00018-017-2670-2> (2018).
23. Conly, J. & Johnston, B. Where are all the new antibiotics? The new antibiotic paradox. *Can. J. Infect. Dis. Med. Microbiol*, **16**, 159–160 <https://doi.org/10.1155/2005/892058> (2005).
24. Zhang, X., Gu, S. & Ding, Y. Simultaneous detection of roxithromycin and dopamine using a sensor platform based on poly(sulfosalicylic acid) and its application in human serum studies. *Anal. Methods*, **6**, 3316–3321 <https://doi.org/10.1039/C4AY00009A> (2014).
25. Qi, M., Wang, P., Cong, R. & Yang, J. Simultaneous determination of roxithromycin and ambroxol hydrochloride in a new tablet formulation by liquid chromatography. *J. Pharm. Biomed. Anal*, **35**, 1287–1291 <https://doi.org/10.1016/j.jpba.2004.04.001> (2004).
26. Lim, J., Jang, B., Lee, R., Park, S. & Yun, H. -i. Determination of roxithromycin residues in the flounder muscle with electrospray liquid chromatography–mass spectrometry. *J. Chromatogr. B: Biomed. Sci. Appl*, **746**, 219–225 [https://doi.org/10.1016/S0378-4347\(00\)00334-0](https://doi.org/10.1016/S0378-4347(00)00334-0) (2000).
27. García-Mayor, M. A., Gallego-Picó, A., Garcinuño, R. M., Fernández-Hernando, P. & Durand-Alegría, J. S. Matrix solid-phase dispersion method for the determination of macrolide antibiotics in sheep’s milk. *Food Chem*, **134**, 553–558 <https://doi.org/10.1016/j.foodchem.2012.02.120> (2012).
28. Castillo-Aguirre, A., Cañas, A., Honda, L. & Richter, P. Determination of veterinary antibiotics in cow milk using rotating-disk sorptive extraction and liquid chromatography. *Microchem. J*, **162**, 105851 <https://doi.org/10.1016/j.microc.2020.105851> (2021).

29. Wang, J., Yang, Z., Wang, X. & Yang, N. Capillary electrophoresis with gold nanoparticles enhanced electrochemiluminescence for the detection of roxithromycin., **76**, 85–90 <https://doi.org/10.1016/j.talanta.2008.02.006> (2008).
30. Wang, H. *et al.* Screening of antimicrobials in animal-derived foods with desorption corona beam ionization (DCBI) mass spectrometry. *Food Chem*, **272**, 411–417 <https://doi.org/10.1016/j.foodchem.2018.08.073> (2019).
31. Ngoc Do, M. H. *et al.* Screening of antibiotic residues in pork meat in Ho Chi Minh City, Vietnam, using a microbiological test kit and liquid chromatography/tandem mass spectrometry., **69**, 262–266 <https://doi.org/10.1016/j.foodcont.2016.05.004> (2016).
32. Zhong, Q. *et al.* One-Pot Synthesis of Highly Stable CsPbBr₃@SiO₂ Core–Shell Nanoparticles. *ACS Nano*, **12**, 8579–8587 <https://doi.org/10.1021/acsnano.8b04209> (2018).
33. Liu, Z. *et al.* Ligand Mediated Transformation of Cesium Lead Bromide Perovskite Nanocrystals to Lead Depleted Cs₄PbBr₆ Nanocrystals. *J. Am. Chem. Soc.*, **139**, 5309–5312 <https://doi.org/10.1021/jacs.7b01409> (2017).
34. Zhang, D. *et al.* A simple extraction method for the simultaneous detection of tetramisole and diethylcarbazine in milk, eggs, and porcine muscle using gradient liquid chromatography–tandem mass spectrometry. *Food Chem*, **192**, 299–305 <https://doi.org/10.1016/j.foodchem.2015.07.014> (2016).
35. Neises, B. & Steglich, W. Simple Method for the Esterification of Carboxylic Acids. *Angew. Chem., Int. Ed. Engl*, **17**, 522–524 <https://doi.org/10.1002/anie.197805221> (1978).
36. Öztürk, N., Akgöl, S., Arısoy, M. & Denizli, A. Reversible adsorption of lipase on novel hydrophobic nanospheres. *Sep. Purif. Technol*, **58**, 83–90 <https://doi.org/10.1016/j.seppur.2007.07.037> (2007).
37. Wang, P., Qi, M. & Jin, X. Determination of roxithromycin in rat lung tissue by liquid chromatography–mass spectrometry. *J. Pharm. Biomed. Anal*, **39**, 618–623 <https://doi.org/10.1016/j.jpba.2005.04.006> (2005).
38. Wan, H., Zhao, F., Wu, W. & Zeng, B. Direct electron transfer and voltammetric determination of roxithromycin at a single-wall carbon nanotube coated glassy carbon electrode. *Colloids Surf. B. Biointerfaces*, **82**, 427–431 <https://doi.org/10.1016/j.colsurfb.2010.09.014> (2011).
39. Peng, J. & Hu, X. A simple fluorescence quenching method for roxithromycin determination using CdTe quantum dots as probes. *J. Lumin*, **131**, 952–955 <https://doi.org/10.1016/j.jlumin.2010.12.030> (2011).
40. Li, C. X. *et al.* Extraction and mechanism investigation of trace roxithromycin in real water samples by use of ionic liquid–salt aqueous two-phase system. *Anal. Chim. Acta*, **653**, 178–183 <https://doi.org/10.1016/j.aca.2009.09.011> (2009).

Figures

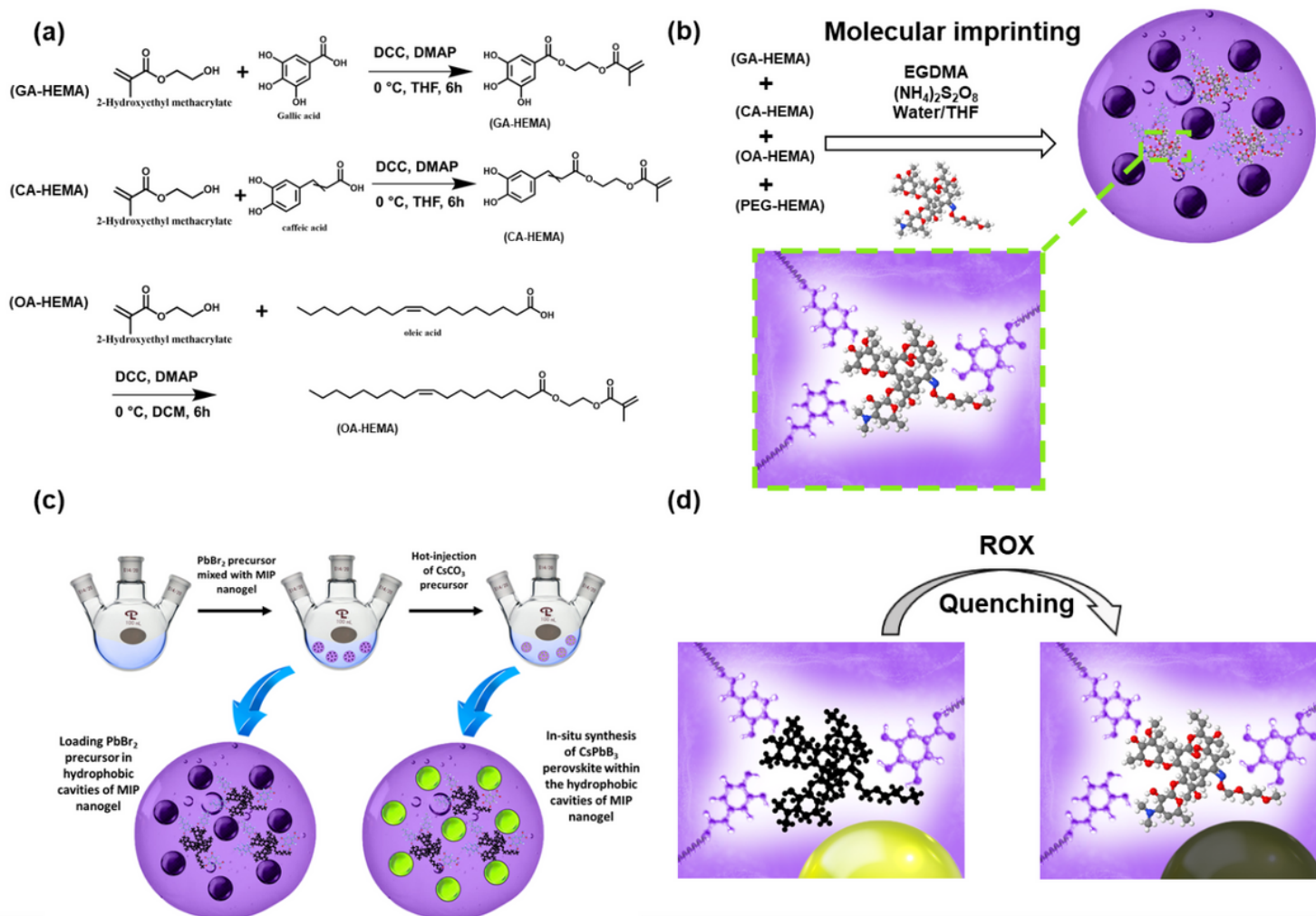


Figure 1

Synthesis and sensing strategies. (a) Synthesis of functional HEMA monomers (b) Synthesis of MIP nanogels (c) Loading of CsPbBr₃ perovskite nanoparticles into MIP nanogels. (d) Sensing of ROX.

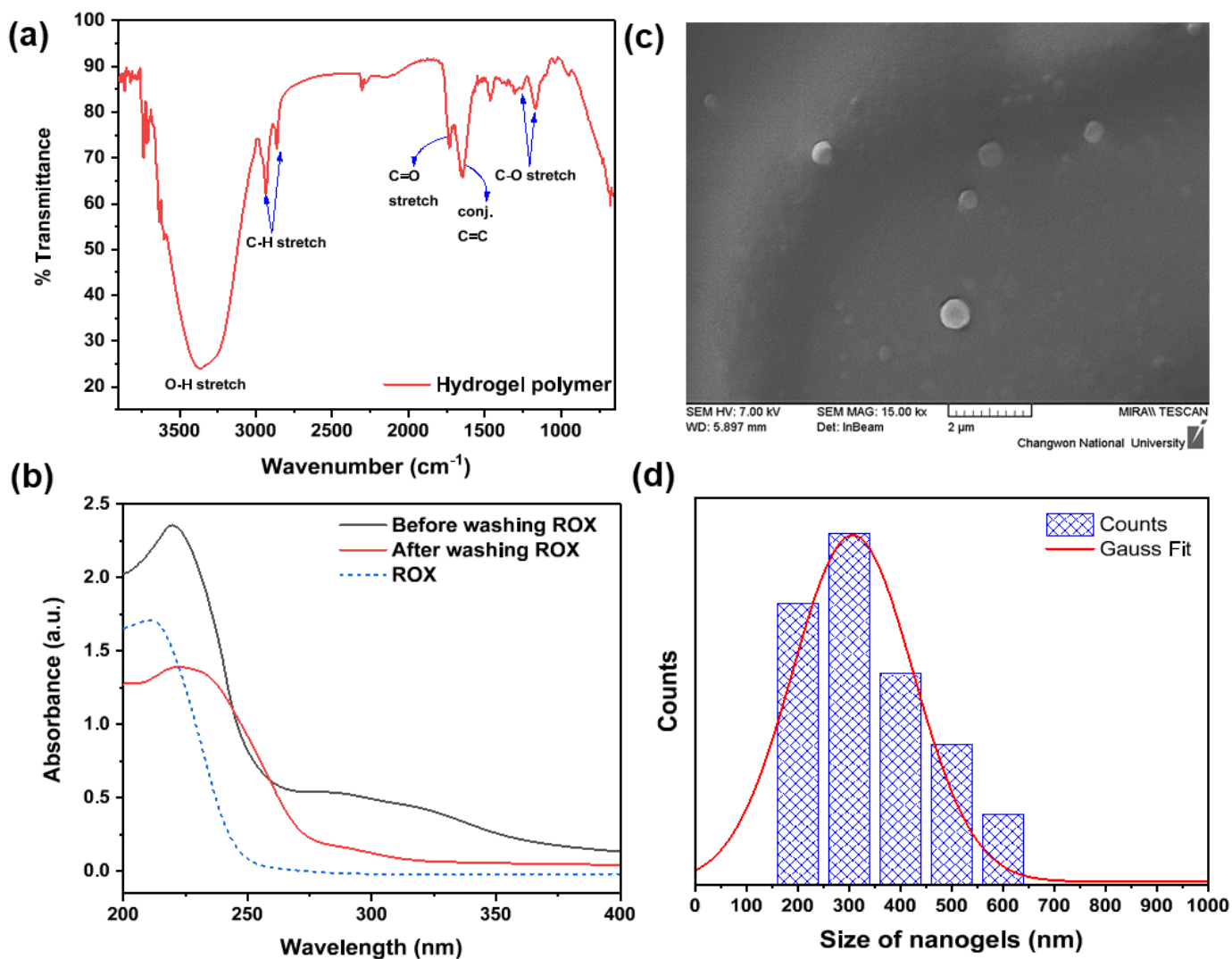


Figure 2

Characterization of MIP nanogels through FTIR (a) and UV-Vis spectrometry (b). FE-SEM image (c) and size distribution of MIP nanogels (d).

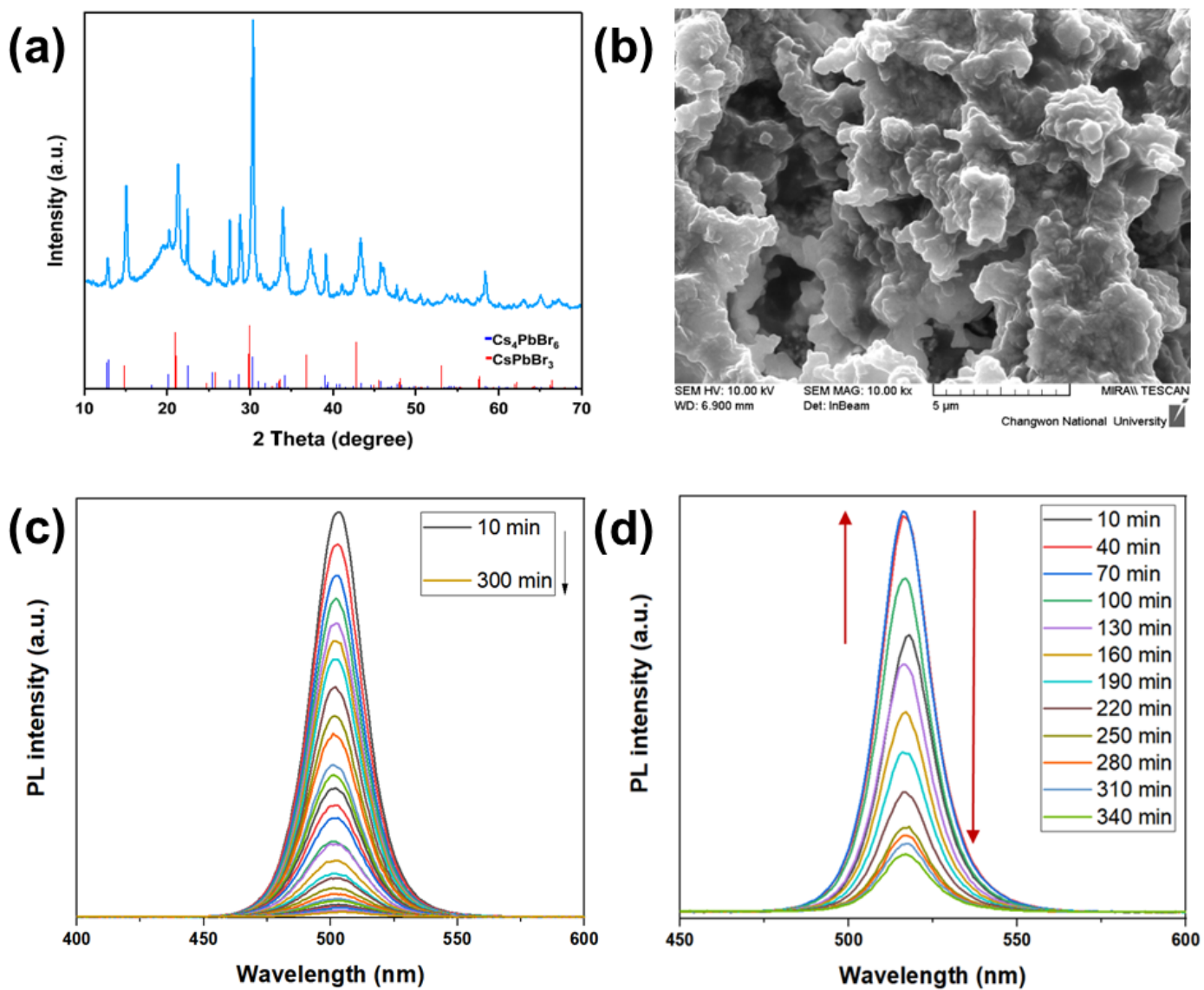


Figure 3

Characterization of perovskite-loaded MIP nanogels by XRD (a) and FE-SEM image(b). PL spectra of perovskite-loaded MIP nanogel in water: nanogel prepared from GA-HEMA: CA-HEMA: OA-HEMA (1 eq: 1eq: 1 eq) (c) and nanogel prepared from GA-HEMA: CA-HEMA: OA-HEMA: PEG-HEMA (1 eq: 1 eq: 1 eq: 3 eq) (d).

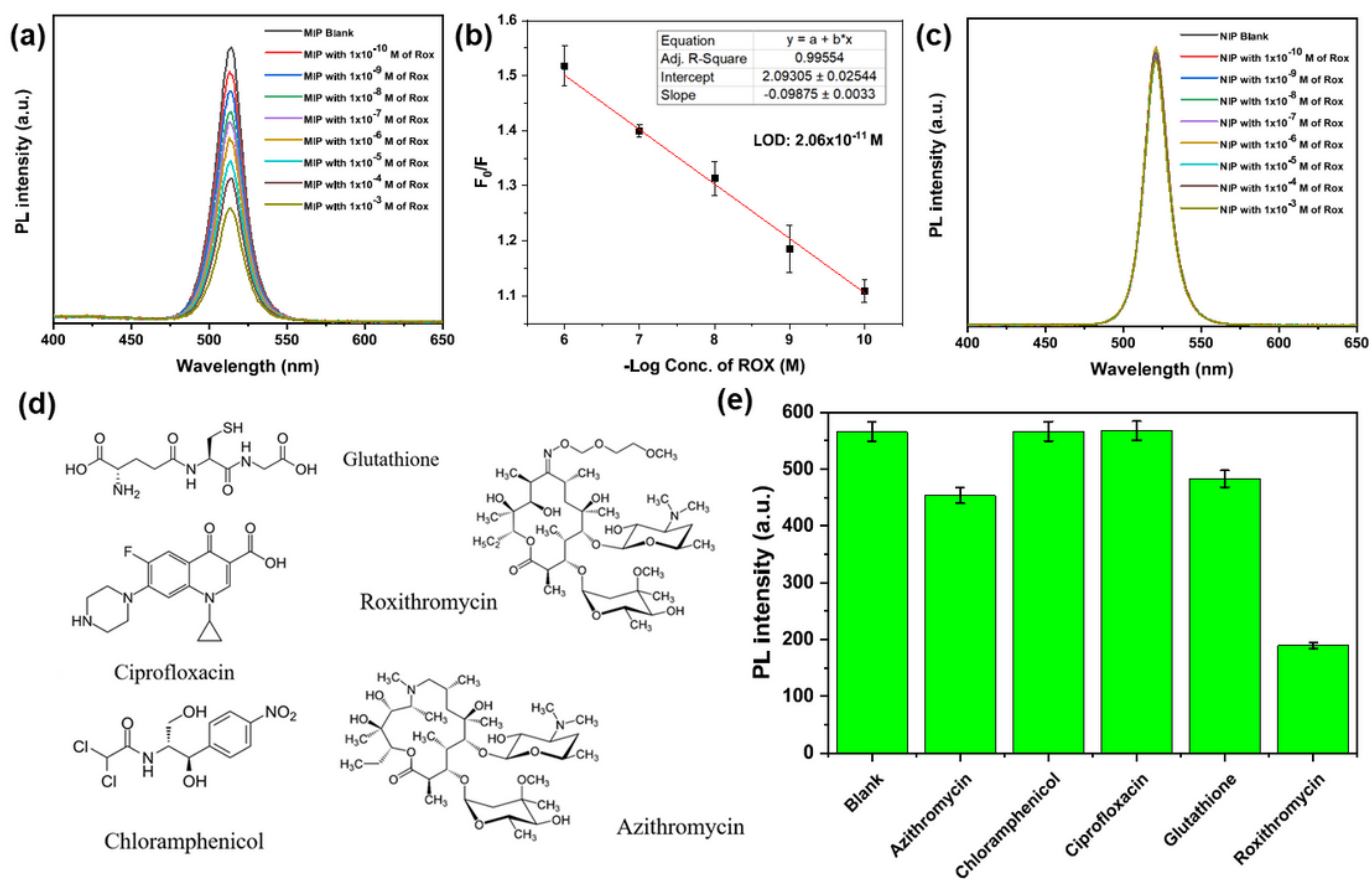


Figure 4

(a) Fluorescence emission spectra of MIP/CsPbBr3 in water containing different concentrations of ROX. (b) The calibration curve of the fluorescence intensity of MIP/CsPbBr3 versus ROX concentrations. (c) Fluorescence emission spectra of NIP/CsPbBr3 in water containing different concentrations of ROX. (d) Chemical structure of analyte tested for selectivity. Fluorescence response of MIP/CsPbBr3 to other analytes (e). All measurements were repeated three times and standard deviations are represented as error bars.

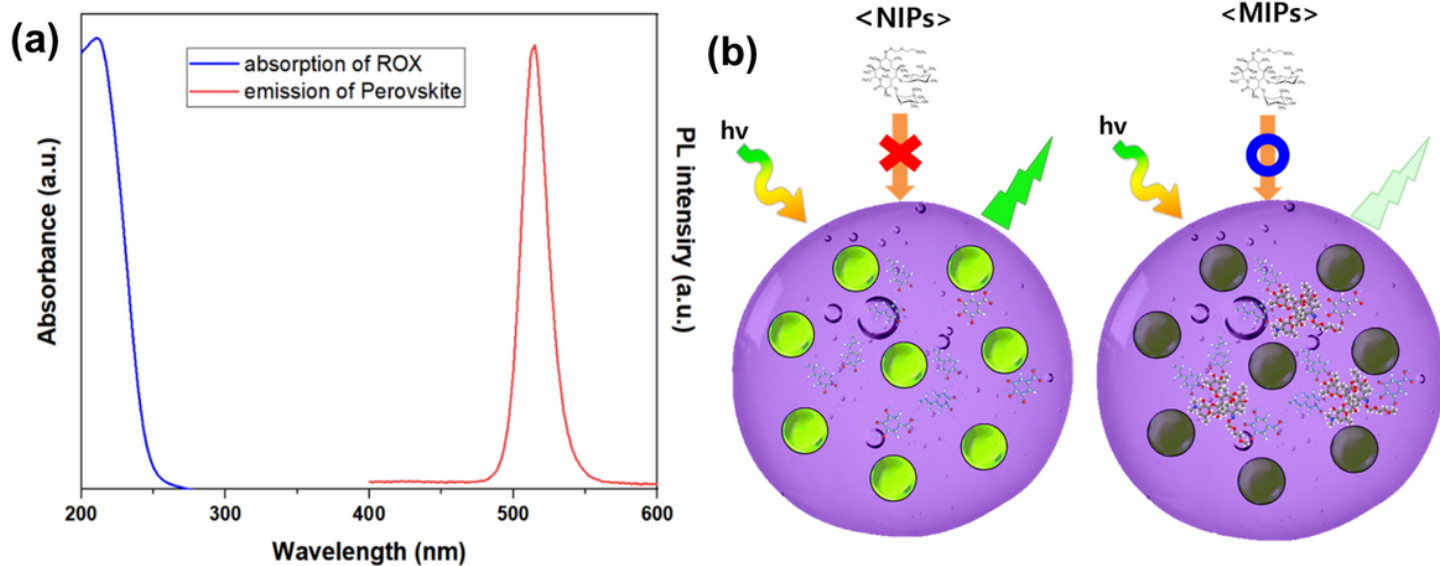


Figure 5

(a) PL and UV spectra of the emission of perovskite and absorption of ROX, (b) Schematic illustration of the proposed quenching mechanism of MIP/CsPbBr₃ during the exposure to ROX.

Supplementary Files

This is a list of supplementary files associated with this preprint. Click to download.

- [Supportinginformation.docx](#)